

THE ROLE OF PARTICLES IN COUNTERFLOW DIFFUSION FLAMES INHIBITED BY IRON PENTACARBONYL^{*}

Marc D. Rumminger[†] and Gregory T. Linteris[‡]
Building and Fire Research Laboratory
National Institute of Standards and Technology
Gaithersburg MD 20899-8651, USA

ABSTRACT

Laser light scattering and thermophoretic sampling have been used to investigate particle formation in a methane-air counterflow diffusion flames inhibited by iron pentacarbonyl ($\text{Fe}(\text{CO})_5$) added to the fuel or the oxidizer stream. Flame calculations, which incorporate only gas-phase chemistry, are used to assist in interpretation of the experimental results. In flames with the inhibitor added to the oxidizer stream, the region of particle formation overlaps with the region of high H-atom concentration, and particle formation may interfere with the inhibition chemistry. When the inhibitor is added to the fuel stream, significant condensation of metal or metal oxide particles is found, which implies that particles prevent active inhibiting species from reaching the region of high radical concentration. As the inhibitor loading increases, the maximum scattering cross section increases sharply, and the difference between the measured and predicted inhibition effect widens, suggesting that particle formation is the cause of the deviation. Thermophoretic sampling in low strain rate flames indicates that the particles have diameters between 5 nm and 25 nm. Thermophoresis affects the nanoparticle distribution in the flames, in some cases causing particles to cross the stagnation plane. The scattering magnitude in the counterflow diffusion flames appears to be strongly dependent on the residence time, and relatively independent of the peak flame temperature.

^{*} Official contribution of the National Institute of Standards and Technology, not subject to copyright in the United States.

[†] National Research Council/NIST postdoctoral fellow 1996-1998. Current address: Ceryx, Inc., Santa Paula, CA 93060.

[‡] Corresponding author. E-mail: linteris@nist.gov. Telephone: 301-975-2283.

INTRODUCTION

Production of the widely used but ozone-destroying compound CF_3Br has been banned, and there remains a need for alternative fire suppressants in a variety of applications. Since some metal compounds have been shown to be up to two orders of magnitude more effective at reducing the burning velocity of premixed flames [1,2], it is of interest to understand their mechanisms of inhibition to determine if there are ways that they might be used as additives to fire suppressant blends, particularly for unoccupied spaces.

In previous research, a gas-phase mechanism for inhibition by $\text{Fe}(\text{CO})_5$ [3] and ferrocene [4] was developed, and it predicted the observed strong inhibition at low inhibitor mole fraction reasonably well for most of the test conditions [5]. For the premixed flames, the dramatic loss of effectiveness of these iron compounds at mole fractions above about 100 ppm^s was shown to be due to the condensation of iron-containing intermediates, and the subsequent formation of particles [6](with particle residence time more important than peak flame temperature). While good progress has been made in understanding the behavior of these compounds in premixed flames [6,7], fires are diffusion flames, and it is important to extend the tests to more representative conditions.

In recent experimental studies with diffusion flames [2], $\text{Fe}(\text{CO})_5$ showed strong inhibition under certain conditions, but almost none under others. Addition of $\text{Fe}(\text{CO})_5$ to the oxidizer stream of a methane-air counterflow diffusion flame produces a large change in the extinction strain rate, whereas addition to the fuel stream yields virtually no effect. Also, the addition to the oxidizer stream illustrates a difference between counterflow diffusion and premixed flames. In premixed flames, there is a dramatic reduction in effectiveness of the $\text{Fe}(\text{CO})_5$ above about 100 ppm, with the burning velocity versus $\text{Fe}(\text{CO})_5$ mole fraction curve appearing very steep below 100 ppm, but nearly flat above that value. Conversely, for counterflow diffusion flames, the extinction strain rate versus $\text{Fe}(\text{CO})_5$ mole fraction curve *does* experience a large change in slope near 100 ppm, but the reduction in the effectiveness of the $\text{Fe}(\text{CO})_5$ is much smaller (i.e. the slope is reduced much less) than in premixed flames. For example, in premixed flames, the slope of the burning velocity curve is reduced by two orders of magnitude above 100 ppm compared to below; whereas in counterflow diffusion flames, the change in slope is much milder, about a factor of 7. In addition, some experiments were performed in diffusion flames of diluted fuel versus oxygen-enriched air. Subsequent numerical modeling of the inhibited counterflow diffusion flames using a gas-phase mechanism [3] explained some of the experimental results, but other effects remain unexplained. For example, the numerical calculations predict much stronger inhibition for many conditions than was observed in the experiments. The goal of the present work is to understand the role of particles in the unexpected loss in effectiveness of $\text{Fe}(\text{CO})_5$ in counterflow flames of undiluted methane and air. Flames with diluted reactants will be addressed in a future paper.

In this paper we investigate iron-species condensation in non-sooting $\text{CH}_4\text{-O}_2\text{-N}_2\text{-Fe}(\text{CO})_5$ counterflow diffusion flames to determine the effect of particle formation on flame

^s All uses of ppm in this paper are on a volume basis and correspond to $\mu\text{mol/mol}$.

inhibition. We use laser-light scattering to determine particle location, and thermophoretic sampling for particle morphology. Calculated flame structures from one-dimensional gas-phase flame models assist in the interpretation of the experimental data and provide insight into the particle formation processes.

EXPERIMENT

Counterflow Burner

The counterflow burner system has been described previously [2,8]. The fuel and oxidizer tubes (22.2 mm diameter) are separated by 11 mm, and there is a nitrogen shroud flow from a concentric cylinder (51 mm diameter) around the bottom (fuel) jet. The burner produces a non-sooting flame with a flat region in the center. The strain rate a (the derivative of the velocity with respect to the axial position) is approximated from the jet exit velocities as $a = (2|V_o|/L) \left(1 + |V_F| \sqrt{\rho_F} / |V_o| \sqrt{\rho_o} \right)$, where L is the jet separation distance, V_i is the velocity of gas i (F =fuel, O =oxidizer), and ρ_i is the density of gas i [9]. The jet exit velocities are chosen so that the momentum of the two streams is balanced at all values of the strain rate; that is, $\rho_F V_F^2 = \rho_o V_o^2$. Iron pentacarbonyl is added to the flames by diverting part of the nitrogen (or methane) stream to a two-stage saturator maintained in a bath at 17 °C to 21 °C, held to within ± 0.5 °C. The gas flow control system and tests to verify carrier gas saturation by $\text{Fe}(\text{CO})_5$ have been described in a previous publication [5].

Optical System

Light-scattering and extinction techniques with phase-sensitive detection are used to determine particle location and properties. The apparatus, shown in Figure 1 is similar to those used by other researchers [10,11]. The light source is a 4-W argon-ion laser (Spectra Physics BeamLok 2060**), with a vertically-polarized 2.2-W beam at 488 nm. A mechanical chopper (Stanford Research 640) modulates the beam at 1500 Hz and provides a reference signal for the lock-in amplifiers. A polarization-preserving single-mode optical fiber (3 μm diameter) carries the light into a chemical fume hood (90 cm x 150 cm x 150 cm) which contains the burner. At the fiber output, collimating optics, a polarization rotator, mirrors and a focusing lens ($f = 250$ mm) deliver the laser light to the test region. A glass wedge between the polarization rotator and the focusing lens diverts a small fraction of the beam to a reference detector which monitors the laser power during the experiments. The transmission efficiency for the laser-to-fiber coupling system is only about 15 %, but this provides sufficient power for the experiments.

The steep temperature gradients in the present flames cause significant beam steering and distortion. These effects, if unmitigated, would produce fluctuations of a few percent in the measured transmissivity, which is approximately the same magnitude as the peak absorptivity (< 2 %). To reduce the beam steering effect, we follow an approach used by

** Certain commercial equipment, instruments, or materials are identified in this paper to adequately specify the procedure. Such identification does not imply recommendation or endorsement by the National Institute of Standards and Technology, nor does it imply that the materials or equipment are necessarily the best available for the intended use.

Dibble [12] and Nguyen [13], which involves reflecting the beam back through the flame along the same path, thus “unsteering” it. The approach has the additional benefit of doubling the path length and nearly doubling the laser light intensity at the focus. A concave spherical mirror ($f = 250$ mm) reflects the beam back through the optical path and a glass wedge sends it to an integrating sphere. To spatially probe the flame, a three-axis translation stage (minimum step size of 0.0016 mm) positions the burner and chimney in the stationary optical path.

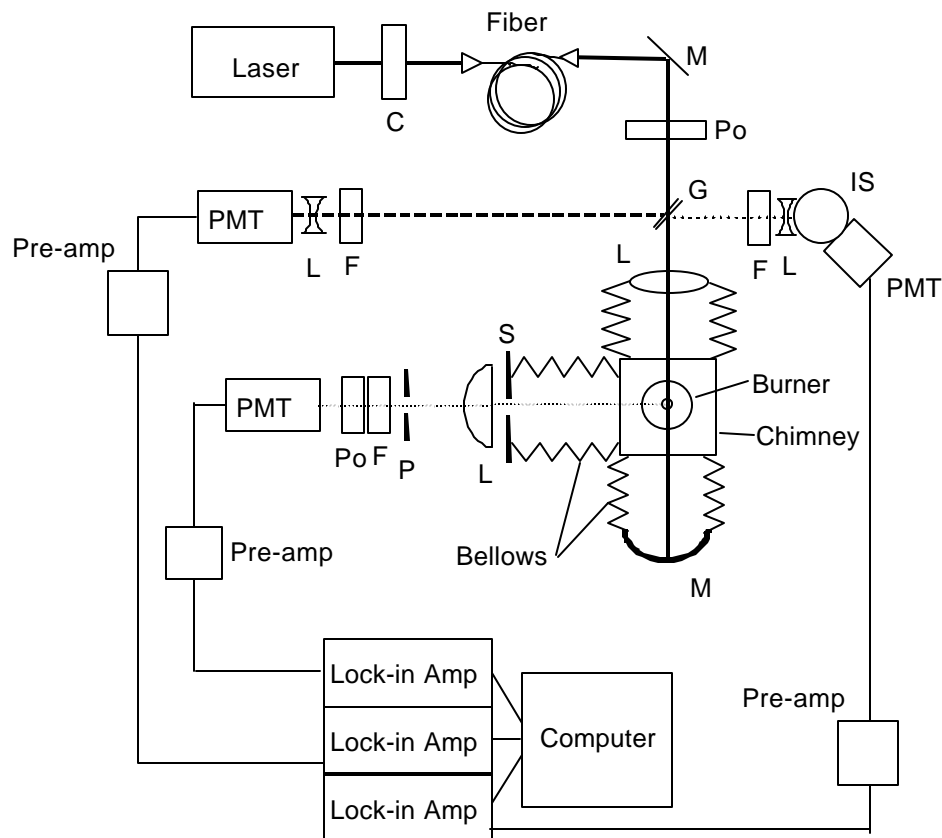


Figure 1 - Schematic of laser scattering/extinction system: C, chopper; M, mirror; G, beam pick-off; L, lens; S, spatial filter (circular aperture); Po, polarizer; F, laser-line and neutral density filters; PMT, photomultiplier; P, pinhole; IS, integrating sphere. (Note: Some structural components are not shown, and the drawing is not to scale.)

The light detection system consists of three photomultiplier tubes (PMT, all type 1P28) with appropriate filtering. The transmitted power is measured using a PMT with neutral density and laser-line (Oriel 52650, $\Delta\lambda = (10 \pm 2)$ nm) filters placed in front of the detector. The reference PMT has neutral density filters ($OD \approx 6$) and a laser-line filter ($\Delta\lambda = (10 \pm 2)$ nm), and is typically operated at a voltage of -500 V. The detection system for light scattered normal to the laser beam consists of a circular aperture (5 mm diameter), collection lens ($f = 100$ mm), pinhole aperture (diameter 1 mm), laser-line filter, polarizer and PMT at -900 V to -1000 V. For the 90° -scattered light, the circular aperture (5 mm diameter) located 10 cm from

the laser beam focus provides a solid angle of 0.002 sr. The pinhole aperture (1 mm diameter) defines the length of the sample to be 1 mm based on unity magnification. The signal from each of the detectors is pre-amplified (Stanford Research 552) before entering a lock-in amplifier (Stanford Research 530). A personal computer controls the amplifiers and records the measurements during the experiments using a data acquisition card (Strawberry Tree DynaRes Ultra 8). In the data acquisition software, each scattering or transmission data point is normalized by the reference signal. Typically, 100 readings are averaged over a time of about 1 s; post-processing software reduces the data and calculates uncertainty as described below. The measured quantities in the experiment are the voltage outputs of the reference, transmission, and scattered light detectors, and these depend on the system geometry, optical efficiencies, detector responsivity, gas density and particle number density, and the scattering cross section of the gases or particles. To obtain the scattering cross section (Q_{vv}) of the gases or particles in the flame, a calibration of the optical system efficiency is performed with blends of CH₄ and N₂ (scattering cross sections of $(18.68 \pm 0.90) \times 10^{-28} \text{ cm}^2$ and $(8.69 \pm 0.37) \times 10^{-28} \text{ cm}^2$ at 488 nm, respectively [14]). The scattering and transmission signals are

measured for the calibration gas to give a calibration factor, $C = Q_{vv,cal} \frac{t_{cal}}{S_{vv,cal}}$, where $Q_{vv,cal}$ is

the known scattering cross section of the calibration gas, t_{cal} is the transmissivity of the calibration gas, and $S_{vv,cal}$ is the scattering signal caused by the calibration gas. Given the calibration constant and scattering measurements, the scattering cross section at each

location can be found as $Q_{vv} = C \frac{S_{vv}}{t_l}$, where S_{vv} is the measured scattering signal and t_l is the

transmissivity of the flame gases and particles. The laser-based measurements are made along a vertical profile at the centerline of the fuel and oxidizer tubes. The path length for the laser extinction measurements (effectively doubled by a retro-reflection technique [6]) is $4.4 \text{ cm} \pm 0.4 \text{ cm}$.

Thermophoretic Sampling

Thermophoretic sampling with electron microscopy is used as a supplemental technique to determine particle size and morphology. The procedure and apparatus are similar to those used by Dobbins and Megaridis [15] and Koylu et al. [16], so limited details will be given here. A computer-controlled, double-acting piston with travel of 5.08 cm is used to quickly insert and remove the electron microscope (EM) grid from the flame. Transit times and the dwell time in the flame are measured using a laser, mirror, photodiode, and oscilloscope [16]. Each grid is attached to a stainless steel substrate with thickness of 0.4 mm, and height between 3 mm to 5.7 mm. The EM grids are copper with a carbon film deposited on one side (Electron Microscopy Sciences p/n CFH4-SPEC-CU), and are fastened onto the metal substrates using adhesive or double-sided tape.

Experimental Uncertainty

The uncertainty analysis consists of calculation of individual uncertainty components and root mean square summation of components [17,18]. All uncertainties are reported as *expanded uncertainties*: $X \pm U$, where U is ku_c , and is determined from a combined standard

uncertainty (estimated standard deviation) u_c , and a coverage factor $k = 2$ (level of confidence approximately 95 %). Likewise, when reported, the relative uncertainty is $U / X \cdot 100 \%$, or $ku_c / X \cdot 100 \%$. The expanded relative uncertainties for the experimentally determined quantities in this study are as follows: 2 % for global strain rate in the counterflow diffusion flames; 5 % for the extinction strain rate; and 11.5 % for $\text{Fe}(\text{CO})_5$ mole fraction.

For the scattering measurements, the combination of steep spatial gradients in the flame, small particle scattering cross section, instability in the flame, and system noise causes the scattering signal to vary about a local mean value at any given location. For each data set (100 points collected in 1 s), the maximum standard deviation of the scattering cross section measurements is generally no more than 10 % of the mean in the region of high Q_{vv} and in the unburned reactants. In some cases, however, such as the Q_{vv} of room temperature air, the maximum standard deviation can be up to 20 %.

RESULTS AND DISCUSSION

Counterflow diffusion flames—as compared with premixed flames—provide a flexible environment for inhibitor addition. In premixed flames, all of the inhibitor flows directly into the reaction zone, whereas in counterflow flames, the amount of the inhibitor that reaches the flame is dependent upon the location of inhibitor addition relative to the locations of the flame and stagnation plane. The flame can be stabilized on either the fuel or oxidizer side of the stagnation plane through suitable dilution of the reactant streams. If the inhibitor is added to the reactant stream on the flame side of the stagnation plane, it will convect directly into the flame; if added to the other side, it must diffuse across the stagnation plane to reach the flame. Additionally, in premixed flames the choice of the reactant mixture fixes the peak temperature and residence time (via burning velocity), whereas in counterflow flames, these can be varied independently of the reactant mixture by varying the jet exit velocities (via the strain rate). Nonetheless, some of the flame properties are coupled to one another. For example, varying the strain rate changes both the temperature field and residence time, and changing the reactant mixtures alters the location of the flame relative to the stagnation plane, and consequently the time-temperature conditions in the flame.

As a result of these features and others, counterflow diffusion flames have been widely used in studies of fire suppressant effectiveness [19-23]. They have also been used as reactors for particle synthesis (see the review of Wooldridge [24] and references therein). Strain rates in synthesis flames have typically been between 10 s^{-1} and 20 s^{-1} , whereas the strain rates used here are 20 to 30 times higher, which results in significantly shorter residence times. While the present results of the effects of particle formation on flame inhibition may also be of use to those studying particle synthesis, the difference in residence time means that some behavior exhibited in typical synthesis flames may not appear in the present flames, and vice versa.

To investigate the effects of flame temperature, residence time, and location of inhibitor addition on particle formation, we employ a methane-air counterflow diffusion flame with two inhibitor addition locations. A stream of methane flowing against air results in a flame on the air side of the stagnation plane (which has a calculated distance of 1 mm from the peak temperature). Numerical calculations (discussed below) predict a peak

temperature of 2020 K at $a=200 \text{ s}^{-1}$ which is lowered to 1786 K at the extinction condition ($a=660 \text{ s}^{-1} \pm 33 \text{ s}^{-1}$). The stoichiometric mixture fraction Z_{st} for this flame is 0.055. Note that Z_{st} quantifies the location of the flame relative to the fuel and air streams. For $Z_{st} = 0.5$, the flame is coincident with the stagnation plane; for $Z_{st} < 0.5$, the flame is on the oxidizer side of the stagnation plane; and for $Z_{st} > 0.5$, the flame is on the fuel side of the stagnation plane.

To describe the flame and inhibitor configuration compactly, we use the notation IX, where “I” refers to the inhibitor, “X” refers to the location of addition (in oxidizer or fuel stream, O or F). For example, IO refers to inhibitor added to the oxidizer stream. In a future paper, we will report on two other flame configurations formed from a stream of diluted fuel flowing against oxygen-enriched air: 13 % CH_4 /87 % N_2 vs. 45 % O_2 /55 % N_2 and 20 % CH_4 /80 % N_2 vs. 30 % O_2 /70 % N_2 . In the following sections, we present results of the scattering cross section measurements, assessments of the effect of the particles on flame inhibition, and extractive measurements of particle diameter for undiluted CH_4 – air flames.

Validation of Calculated Temperature Field

In previous work, flame inhibition by $\text{Fe}(\text{CO})_5$ in diffusion flames has been studied through measurements of global properties (reactant flows at extinction) [2]. The structures of the flames have been calculated based on a detailed kinetic model, and some validation of the kinetic mechanism has been provided by comparisons between measured and calculated global properties of premixed and diffusion flames [3,5,7,25]. Clearly, detailed measurements of the flame structure can provide the best validation of the mechanism, and while they are desired, they are not yet available for flames inhibited by $\text{Fe}(\text{CO})_5$. Nonetheless, we use the calculations to interpret the present particle measurements. In particular, the calculations provide an estimate of the temperature profile, as well as the region of high radical mole fraction and subsequent high activity of the gas-phase iron species catalytic radical recombination cycles. Consequently, we seek a simple method to experimentally validate some major features of the predicted flame structure.

The temperature profile can be calculated *from* the experimentally obtained Rayleigh scattering by the cold reactant and hot product gases (data which are obtained during the present experiments). This, however, requires knowledge of the exact species mole fractions at each position in the flame (since it is not possible to separate changes in scattering cross section caused by temperature variation from those due to changes in chemical composition). Alternatively, we can compare the experimental and calculated temperature profiles indirectly, by evaluating the calculated and measured scattering cross sections. The calculations for flame structure are performed using a flame code from Smooke [26], which uses the *Chemkin* [27] and the transport property subroutines [28], and a one-carbon chemical mechanism [29]. At each grid point in the flame, we calculate the density-weighted

scattering cross section $Q_{vv,j} = e_o \sum_{i=1}^{ii} \sigma_i X_{i,j} (1/T_j)$, where e_o is the empirically-determined optical efficiency coefficient ($\text{K}/\text{cm}^3\text{-sr}$), σ_i is the Rayleigh cross section of the i -th species (cm^2), $X_{i,j}$ is the mole fraction of the i -th species at the j -th grid point, and T_j is the temperature at the j -th grid point (K). We consider only the major species CH_4 , N_2 , O_2 , CO_2 and H_2O in the summation, and use cross section data from Ref. [14] (CH_4 , N_2) and Ref. [30] (O_2 , CO_2 , and H_2O). We obtain the optical efficiency coefficient of the experimental set-up by a best-fit to the signals from the inlet reactants at the air and fuel jet exits. A comparison of

the calculated and measured cross section for an uninhibited flame at $a = 330 \text{ s}^{-1}$ is shown in Figure 2. Qualitative agreement is good, notably in terms of the location of initial decrease in Rayleigh cross section, and the location of minimum cross section (i.e., maximum temperature). Despite the discrepancy in the absolute Q_{vv} (caused mainly by stray scattered light), we can use the numerical calculations to assist in interpretation of the experimental data. For example, the calculations can be used to identify the *spatial* locations of various features for the scattering data, such as the stagnation plane and the region of high temperature.

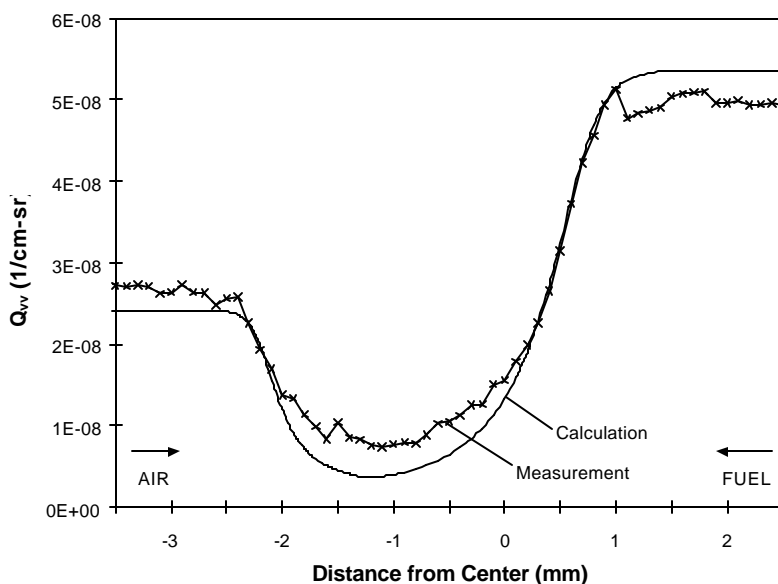


Figure 2: Comparison of calculated and measured Q_{vv} for uninhibited flame at $a = 330 \text{ s}^{-1}$.

Inhibitor in the Oxidizer (IO)

Figure 3 shows the measured scattering cross section (Q_{vv}) together with the calculated temperature (upper x-axis), H-atom mole fraction, and stagnation plane location for CH_4 -air flame with inhibitor in the oxidizer (IO). The strain rate is 330 s^{-1} , which is $(50 \pm 2.5) \%$ of the extinction strain rate. Unlike in premixed flames, the “thickness” (indicated by the region of increased temperature) of a counterflow flame (when far from the extinction condition) is unaffected by addition of the inhibitor [25]; hence, the Q_{vv} profile of the uninhibited flame (from Rayleigh scattering by the hot products and cold reactants) is a good marker for the flame location. The hatched horizontal line near the top of the figure shows the estimated residence time τ_{res} (via 10 ms intervals between hatch marks). The estimation encompasses the gas and thermophoretic velocities (assuming 5 nm particles) as discussed below. Note that near the particle stagnation region, the near-zero particle velocities create very large uncertainties in the estimated residence time. This region (caused in part by the limited resolution of the numerical flame structure calculation) is indicated by a shaded bar.

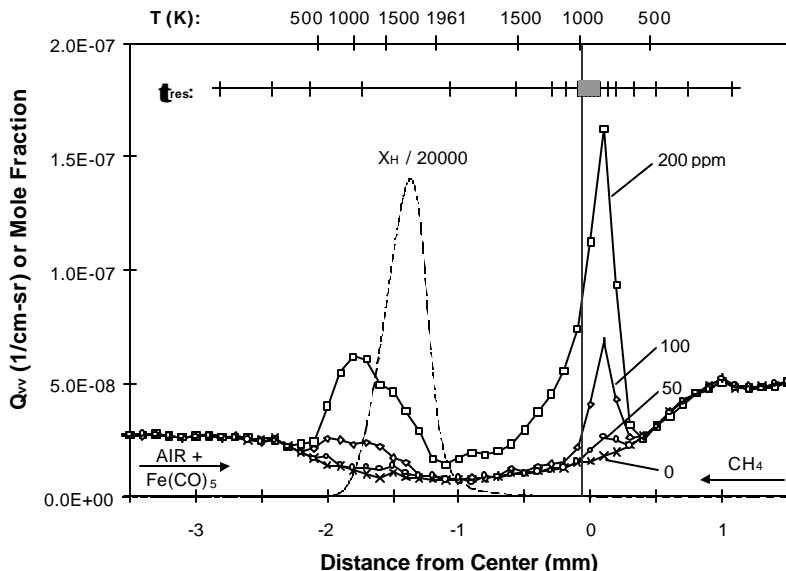


Figure 3: Methane-air counterflow diffusion flame with inhibitor in the oxidizer (IO). Shown are the calculated temperature (upper scale), stagnation plane location (vertical line), and H-atom mole fraction (dashed line) for the uninhibited flame, and the measured scattering profiles (connected points) for $\text{Fe}(\text{CO})_5$ mole fractions of (0, 50, 100 and 200) ppm in the air stream ($a = 330 \text{ s}^{-1}$, which is 50 % of a_{ext} for the uninhibited flame and 77 % of a_{ext} for $X_{\text{in}} = 200 \text{ ppm}$). The estimated residence time for 5 nm particles is shown as 10 ms intervals in the hatched line near the top.

At each inhibitor concentration, there are three distinct regions in the flame: 1) a region of particles on the oxidizer side of the flame, 2) a nearly particle-free region near the point of peak temperature, and 3) a region of particles on the fuel side of the flame. As the inhibitor mole fraction increases from 50 ppm to 200 ppm, the scattering increases strongly on both sides of the flame, with a faster increase on the fuel side. This strong dependence of scattering on additive concentration has been observed previously [31,32]. Also, a double-peaked scattering profile like that in Figure 3 has been observed in $\text{H}_2\text{-O}_2$ counterflow diffusion flames with added $\text{Al}(\text{CH}_3)_3$ and TiCl_4 [33], and VOCl_3 and PCl_3 [34]. In those studies, both peaks occur in a region of monotonically rising temperature, and are thought to be a result of changes in particle structure from chains of small particles to relatively large spheres. Possible reasons for appearance of two peaks in the present flames are described below.

Examination of the Q_{vv} and calculated temperature (upper x-axis) provides an explanation for the twin-peaked Q_{vv} structure. Inhibitor, entering with the air, decomposes into Fe and CO upon heating. Some of the Fe immediately condenses (or possibly oxidizes and then condenses) resulting in formation of the first peak ($-2.1 < z < -1.8$, where z is the distance from the center of the nozzles). The temperature continues to increase ($-1.8 < z < -1.2$), which may cause a reduction of particle size or number density, reducing the scattering

cross section. As the gas cools on the fuel side of the peak temperature ($-1.2 < z < 0.4$), the particles reappear and the scattering cross section increases. Since the gas velocity drops as the stagnation plane is approached, the residence time increases and particles grow larger or agglomerate. It is also possible that the different peak heights on the fuel side and air side are caused by thermophoretic redistribution of particles or changing gas composition and the resulting difference in nucleation behavior [31].

We can use the results shown in Figure 3 to infer the effect of the particles on flame inhibition. The appearance of particles on the oxidizer side is most significant, since that is where the inhibition reactions are believed to be occurring [25]. Hydrogen atom is the radical most scavenged by the iron compounds, so its profile serves as a marker of the region of important inhibition chemistry (note that the location of the peak H-atom profile is the same for inhibited and uninhibited flames [25]). The overlap between the H-atom profile and the regions of increased scattering is significant (especially at 200 ppm), and suggests that particle formation influences the inhibition chemistry since the particles are likely composed of inhibiting species from the gas phase. The fuel-side peak probably has little effect on the inhibition chemistry since the loss of active species to particles on the fuel side is beyond the region of chemical influence.

At first glance, it is surprising in Figure 3 that fuel-side peaks occur, since these require particles (or their precursors) to cross the stagnation plane. Their location, however, may be a result of thermophoretic movement of the particles to the region of lower temperature. We can evaluate this possibility by employing the counterflow flame model. The thermophoretic velocity of a particle can be estimated at each location in the flame via $V_T = (\alpha_T D)_p \cdot (-\nabla T/T)$, where α_T is the (dimensionless) thermophoretic diffusion factor, D is the particle Brownian diffusivity, T is the local temperature, P is the pressure, and ∇T is the local temperature gradient [35]. Waldmann and Schmidt [36] used kinetic theory to develop an approximation for $(\alpha_T D)_p$ which applies to the free molecular regime ($\text{Kn} \gg 1$, where Kn is the ratio of the mean free path to the particle radius): $(\alpha_T D)_p = (3/4) \cdot [1 + (P/8 \cdot \alpha)]^{-1} \cdot n$, where α is the tangential momentum accommodation coefficient (which we set equal to unity, as justified by Talbot et al. [37]), and ν is the kinematic viscosity (momentum diffusivity) of the local gas mixture (calculated using the *Chemkin* transport libraries [28]). Our measurements suggest that the particles are in the free molecular regime (see the Particle Morphology section below). Figure 4 shows calculated gas velocity (V_{gas}) along with the negative of the thermophoretic velocity, and the measured Q_{vv} for $X_{\text{in}}=200$ ppm. Near the air-side scattering peak, $|V_T|$ is four times smaller than $|V_{\text{gas}}|$, implying that thermophoresis has a minor effect on the shape of the particle field. Near the fuel-side scattering peak, however, $|V_T| > |V_{\text{gas}}|$, so that thermophoresis has likely caused the particles on the fuel side of the flame to cross the stagnation plane and move upstream. These results have relevance for material synthesis in counterflow flames. Thermophoretic effects could potentially be used to isolate nascent particles in oxidizing or reducing sections of the counterflow reactor, or could be used as an additional control of the residence time for particle growth. Alternatively, thermophoresis could lead to particle contamination as particles remain in the wrong part of the flame for too long.

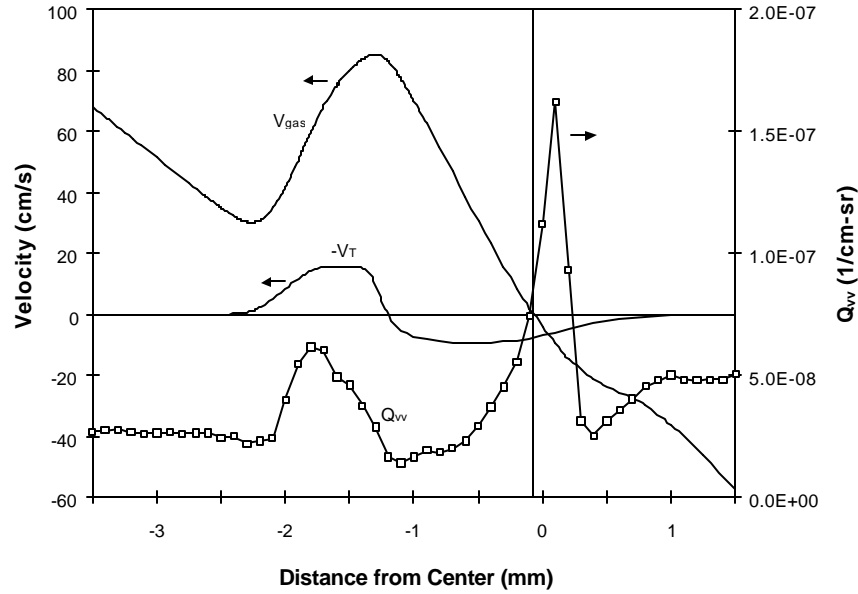


Figure 4: Measured Q_{vv} , calculated gas velocity V_{gas} , and negative of the thermophoretic velocity ($-V_T$) for case IO. Values of $-V_T > 0$ correspond to particles moving to the left. The vertical line marks the stagnation plane. The location of $V_T=0$ at $z=-1.2$ mm corresponds to the point of peak temperature. $a = 330 \text{ s}^{-1}$, $X_{in} = 200 \text{ ppm}$.

One of the primary motivations for the present particle measurements is to understand why the numerical calculations using the gas phase mechanism significantly overpredict the inhibition by $\text{Fe}(\text{CO})_5$ in IO flames. As described in Ref. [3], the inhibition calculated using a gas-phase mechanism is within experimental uncertainty for X_{in} below about 50 ppm, but above that value the model predicts too much inhibition. It has been proposed that particle formation is a reason for the discrepancy, so it is of interest to see how particle formation and the deviation between model and experiment correlate.

In order to compare the presence of particles and the strength of the flame inhibition, we must define suitable parameters describing each variable. The extinction strain rate (a_{ext}) is defined by the global relationship above using the jet exit velocities at which the flame extinguishes, and a_{ext} can be used as a measure of the effect of the inhibitor on the overall reaction rate, since with added $\text{Fe}(\text{CO})_5$, the flame location does not change significantly. (As described previously [22], changes in the flame location with inhibitor addition can change the scalar dissipation rate—which is a truer measure of the characteristic chemical time than the extinction strain rate). For the ‘particle parameter,’ we desire a measure of the presence of particles at (or very close to) the extinction condition. In the present work, we use the peak scattering cross section Q_{vv} as an estimate of the particle quantity (since other measurements of particle loading are difficult in the present flames, as described below). Also, for the IO flames, we only examine the oxidizer-side peak since formation of particles on the fuel side of the flame is downstream of the location where the important inhibition chemistry is believed to be occurring.

In principle, we could determine the scattering cross section very close to extinction. Such measurements are difficult, however, since the flame is unstable there. Alternatively, measurements at a fixed strain rate (Figure 3) are possible, but would be inappropriate because at $a=330 \text{ s}^{-1}$ the 0 ppm flame is far from extinction while the 200 ppm flame is close to extinction, and the scattering signal decreases as one gets close to extinction. As an illustration, for a flame with 200 ppm of $\text{Fe}(\text{CO})_5$, increasing the strain rate from 150 s^{-1} to 350 s^{-1} decreases the air-side peak Q_{vv} by a factor of 2.9. (This occurs despite the decrease in peak temperature which accompanies the increase in strain rate, suggesting that for these conditions, particle formation depends more upon changes in the residence time than the peak temperature.) It is possible to gain some understanding of behavior near extinction by examining the behavior at stable strain rates which are below extinction, and then extrapolating to the strain rate at extinction. The extrapolated peak Q_{vv} at the extinction strain rate of 660 s^{-1} is $6 \times 10^{-8} \text{ cm}^{-1} \text{ sr}^{-1}$ and $9 \times 10^{-8} \text{ cm}^{-1} \text{ sr}^{-1}$ on the air and fuel side, respectively. These values are still significantly above the Q_{vv} from the reactant gases in the uninhibited flame at the same spatial location ($\approx 2 \times 10^{-8} \text{ cm}^{-1} \text{ sr}^{-1}$), implying that the particles do not completely disappear at the extinction point. It is most appropriate to choose flames that are at the same *relative strain rate* with respect to extinction (a/a_{ext}), as close as possible to extinction. As a compromise, for our correlation of the particle scattering with the degree of chemical inhibition, we make our scattering measurements at 75 % of the extinction strain rate, as listed in Table 1.

Figure 5 shows the correlation between inhibition (measured and predicted normalized extinction strain rate) and particle formation (peak Q_{vv}) for the IO flame (the calculated and experimental extinction strain rates are each normalized by their uninhibited value). At $X_{in}=100 \text{ ppm}$, where the model predictions are close to the experimental results, there is little more scattering in the inhibited flames than in the uninhibited flame. (The Q_{vv} of the uninhibited flame, from Rayleigh scattering from the gas molecules is roughly $10^{-8} \text{ cm}^{-1} \text{ sr}^{-1}$ at the location of the Q_{vv} peaks in the inhibited flames.) As X_{in} increases and the difference between the measured and predicted extinction strain rate widens, the maximum Q_{vv} increases sharply, thus suggesting that particle formation is the cause of the deviation. As in the premixed flames [6], the active inhibiting species are being lost to the condensed phase particles (which remove radicals at a much slower rate, if at all). While it has been proposed [25] that the reduced effectiveness at high X_{in} could be a result of saturation of the catalytic cycles (due to radical mole fractions approaching equilibrium values and a smaller radical pool), the inhibitor loses its effectiveness more drastically in the experiments than in the calculations (which include the effects of catalytic cycle saturation).

Table 1 : Measured values of $0.75 \cdot a_{\text{ext}}$ for various inhibitor loadings. Relative uncertainty of $0.75 \cdot a_{\text{ext}}$ is $\pm 5 \%$.

Fe(CO) ₅ (ppm)	a (s ⁻¹)
0	495
25	478
50	431
100	386
200	323
300	298
400	282
500	255

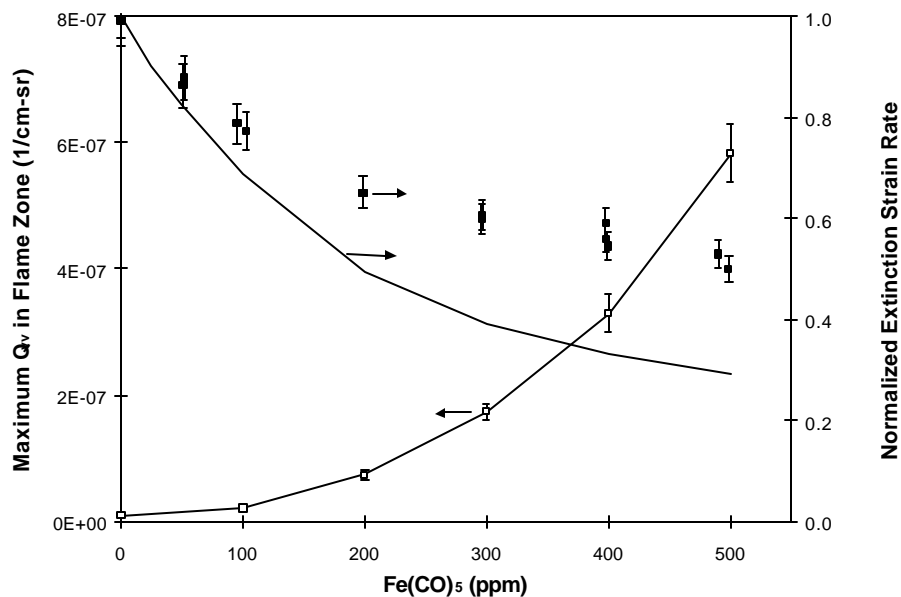


Figure 5: Correlation between inhibition effect and maximum Q_{vv} (case IO). Filled points are experimental normalized a_{ext} , solid line are calculated a_{ext} ([3]). Open connected symbols are maximum measured Q_{vv} . Particle data collected at 75 % of a_{ext} (see Table 1).

One unexplained difference between the premixed and counterflow results is that the premixed flames have a nearly flat leveling-off behavior at high X_{in} , while in the counterflow flames (filled squares in Figure 5) the slope is only reduced. While it is difficult to infer the reasons without detailed modeling of the condensation process, differences in the time-temperature history of the particles may *retard* particle formation in the counterflow flames. For example, at higher X_{in} , the peak temperature is higher and the residence time is lower at a_{ext} , both of which reduce particle formation rates. Thus, in these counterflow diffusion flames, as inhibitor is added, properties of the flame are modified so as to retard particle formation. Conversely, in premixed flames, as X_{in} increases, the peak temperature is relatively unchanged, but the residence time increases (due to the lower burning velocity), so that flame characteristics for particle formation are *enhanced*. It is noteworthy that for methane and air with 300 ppm of added $\text{Fe}(\text{CO})_5$, premixed flames—which lose their effectiveness more dramatically than do counterflow flames—have a peak scattering signal about twice that of the counterflow flames.

Inhibitor in the Fuel Stream (IF)

With the flame on the oxidizer side of the stagnation plane, addition of $\text{Fe}(\text{CO})_5$ to the fuel stream results in no appreciable inhibition [2]. Although a case has been made (using a numerical model with a gas-phase chemical mechanism) that transport of the inhibiting molecules to the region of high radical concentration is the most important factor [25],

particle formation may have an additional effect. Consequently, scattering cross section measurements were made in flames with inhibitor added to the fuel stream.

Figure 6 shows the scattering cross section resulting from addition of $\text{Fe}(\text{CO})_5$ (0 to 300 ppm) to the fuel stream. Most of the scattering occurs on the fuel side of the stagnation plane ($z \approx 0.25$ mm), far away from the point of peak H atom ($z \approx -1.4$ mm). Although this implies that there is no direct overlap between the particle and high radical mole fraction regions, the particles still act as a sink for the inhibiting species, and reduce the number of iron-containing molecules that are available to diffuse through the flame to the region of high radical concentration.

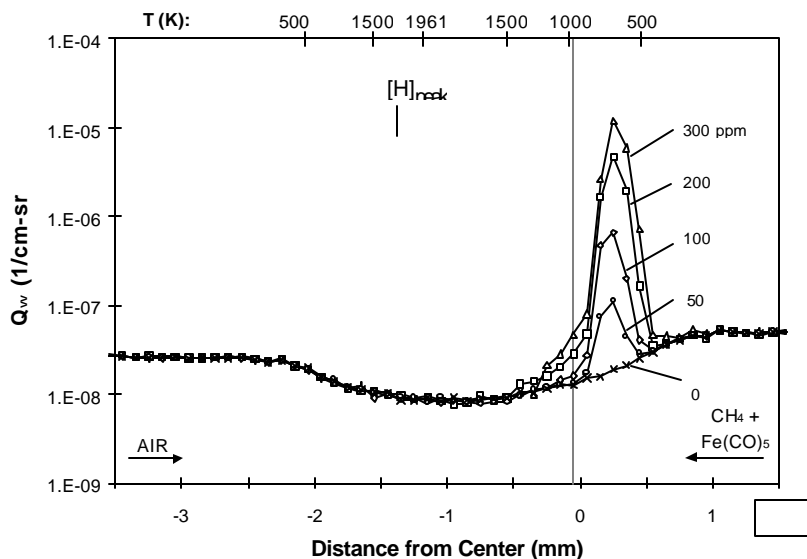


Figure 6: Measured scattering profiles in CH_4 -air counterflow diffusion flame with inhibitor in the fuel (case IF). The calculated temperature and point of peak H-atom mole fraction are marked on the upper x-axis, and the vertical line denotes the calculated location of the stagnation plane. Strain rate = 330 s^{-1} .

The peak Q_{vv} is strongly dependent on X_{in} , but the spatial location of the peak value is independent of X_{in} , a behavior that was previously seen for silica particle synthesis in H_2 - O_2 counterflow diffusion flames [31]. Compared to scattering cross section profiles for the IO flame in the previous section, only one peak appears and the maximum Q_{vv} is about 30 times larger. The value of the peak Q_{vv} may be higher because the fuel-side particles have a relatively long residence time, which is due to a combination of low gas velocity near the stagnation plane and a thermophoretic force which opposes the convective flow.

Particle Morphology

Figure 7 shows a transmission electron microscopy (TEM) image of particles sampled from the low strain ($a=150 \text{ s}^{-1}$) counterflow diffusion flame with $\text{Fe}(\text{CO})_5$ inhibitor added to the

oxidizer stream (IO). In general, the degree of agglomeration is much smaller than that of the premixed flame [6]. Primary particle sizes range from 5 nm to 25 nm in diameter.

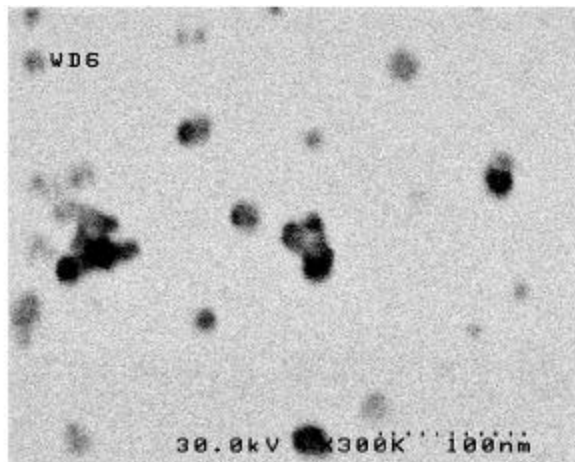


Figure 7: Electron micrograph of iron-containing particles extracted from counterflow diffusion flame at $a = 150 \text{ s}^{-1}$ and $X_{in} = 300 \text{ ppm}$.

CONCLUSIONS

Particle formation in a counterflow diffusion flame of $\text{CH}_4\text{-N}_2\text{-O}_2$ inhibited by $\text{Fe}(\text{CO})_5$ added to the fuel or the oxidizer stream has been studied. Numerically calculated Rayleigh cross sections agree well with the experimentally measured values for uninhibited flames, and support the use of calculated flame structures for assisting in interpretation of the experimental data. Thermophoretic sampling and transmission electron microscopy showed the particles to have primary particle diameters of 5 to 25 nm, with only slight agglomeration.

The particle scattering measurements in the counterflow diffusion flames suggest that particle formation reduces the inhibition effect of $\text{Fe}(\text{CO})_5$, and that the time-temperature history of the particles has a large effect on their formation rate (and hence the inhibitor's loss of effectiveness), as opposed to the peak flame temperature. The time-temperature history of the nascent particles is most dependent upon the location of the flame (i.e. the peak temperature) relative to location of agent addition and the flow stagnation plane. Thermophoresis can also have a large effect on the particle velocity. The measurements indicate that if the iron-containing intermediate species (which are believed to enter into the radical recombination reactions) are lost to a condensed phase, they can become unavailable to interact with the radicals in regions where they affect the overall reaction rate. This can occur either through direct loss to the condensed phase where the peak radical mole fractions occur, or through particle formation upstream and subsequent convection of the particles away from the location of high radical mole fraction.

The present measurements in these laboratory flames have implications for both fire suppression and flame particle synthesis. For fire suppression, it is important for gas-phase chemical inhibitors to stay in the gas phase. If conditions permit loss of the inhibiting species

to a condensed phase and their subsequent convection away from regions of radical chain branching, the inhibitor may be much less effective. It may be advantageous to use low, non-condensing mole fractions of multiple inhibitors.

For particle synthesis, it may be important to control the flame location and temperature field (changeable through reactant dilution), the gas velocity, and the location of precursor addition to optimize the desired residence time in the appropriate chemical environment. For example, the proximity of the peak temperature to the stagnation plane can drastically affect the residence time in the low, moderate, and high temperature regions of the flames, through convection or thermophoresis.

The authors thank undergraduate student intern Nikki Prive for assistance with data acquisition and uncertainty analysis programs and Maria Aquino for operating the electron microscope and advising us on sampling techniques. Discussions with Dr. George Mulholland about particle measurement techniques and Dr. Quang-Viet Nguyen about beam steering contributed greatly to this work. This research is part of the Department of Defense's Next Generation Fire Suppression Technology Program, funded by the DoD Strategic Environmental Research and Development Program (SERDP).

REFERENCES

- [1]. Lask, G. and Wagner, H.G., *Proceedings of the Combustion Institute*, Vol. 8, Williams and Wilkins Co., Baltimore, 1962, pp. 432-438.
- [2]. Reinelt, D. and Linteris, G.T., *Proceedings of the Combustion Institute*, Vol. 26, The Combustion Institute, Pittsburgh, 1996, pp. 1421-1428.
- [3]. Rumminger, M.D., Reinelt, D., Babushok, V., and Linteris, G.T., *Combust. Flame* 116:207 (1999).
- [4]. Linteris, G.T., Rumminger, M.D., Babushok, V.I., and Tsang, W., *Proceedings of the Combustion Institute*, Vol. 28, The Combustion Institute, Pittsburgh, PA, 2000, pp. (accepted).
- [5]. Rumminger, M.D. and Linteris, G.T., *Combust. Flame* 120:451 (2000).
- [6]. Rumminger, M.D. and Linteris, G.T., *Combust. Flame* 123:82 (2000).
- [7]. Linteris, G.T., Rumminger, M.D., and Babushok, V.I., *Combust. Flame* 122:58 (2000).
- [8]. Puri, I.K. and Seshadri, K., *Combust. Flame* 65:137 (1986).
- [9]. Seshadri, K. and Williams, F.A., *Int. J. of Heat and Mass Transfer* 21:137 (1978).
- [10]. Charalampopoulos, T.T., Hahn, D.W., and Chang, H., *Appl. Opt.* 31:6519 (1992).
- [11]. Santoro, R.J., Semerjian, H.G., and Dobbins, R.A., *Combust. Flame* 51:203 (1983).
- [12]. Nguyen, Q.-V., Ph.D. Dissertation, University of California, Berkeley, 1995.
- [13]. Dibble, R. W., Ph.D. Dissertation, University of Wisconsin, Madison, 1975.
- [14]. Rudder, R.R. and Bach, D.R., *Journal of the Optical Society of America* 58:1260 (1968).
- [15]. Dobbins, R.A. and Megaridis, C.M., *Langmuir* 3:254 (1987).
- [16]. Koylu, U.O., Mecnally, C.S., Rosner, D.E., and Pfefferle, L.D., *Combust. Flame* 110:494 (1997).
- [17]. Taylor, B. N. and Kuyatt, C. E., *Guidelines for Evaluating and Expressing the Uncertainty*

- of NIST Measurement Results*, National Institute of Standards and Technology, NIST Technical Note 1297, 1994.
- [18]. Moffat, R.J., *Transactions of the ASME* 104:250 (1982).
 - [19]. Milne, T.A., Green, C.L., and Benson, D.K., *Combust. Flame* 15:255 (1970).
 - [20]. Masri, A.R., *Combust. Sci. Technol.* 96:189 (1994).
 - [21]. Hamins, A., Trees, D., Seshadri, K., and Chelliah, H.K., *Combust. Flame* 99:221 (1994).
 - [22]. Fallon, G.S., Chelliah, H.K., and Linteris, G.T., *Proceeding of the Combustion Institute*, Vol. 26, The Combustion Institute, Pittsburgh, 1996, pp. 1395-1403.
 - [23]. Zegers, E.J.P., Williams, B.A., Fisher, E.M., Fleming, J.W., and Sheinson, R.S., *Combust. Flame* 121:471 (2000).
 - [24]. Wooldridge, M.S., *Prog. Energy Combust. Sci.* 24:63 (1998).
 - [25]. Rumminger, M.D. and Linteris, G.T., *Fire Safety Science: Proceedings of the Sixth International Symposium*, International Association for Fire Safety Science, Marne-La-Vallee, France, 2000, pp. 289-300.
 - [26]. Smooke, M.D., Puri, I.K., and Seshadri, K., *Proceedings of the Combustion Institute*, Vol. 21, The Combustion Institute, Pittsburgh, 1986, pp. 1783-1792.
 - [27]. Kee, R. J., Rupley, F. M., and Miller, J. A., *CHEMKIN-II: A Fortran Chemical Kinetics Package for the Analysis of Gas Phase Chemical Kinetics*, Sandia National Laboratory, SAND89-8009B, 1989.
 - [28]. Kee, R. J., Dixon-Lewis, G., Warnatz, J., Coltrin, R. E., and Miller, J. A., *A Fortran Computer Package for the Evaluation of Gas-Phase, Multicomponent Transport Properties*, Sandia National Laboratory, SAND86-8246, 1986.
 - [29]. Peters, N., in *Reduced Kinetic Mechanisms for Applications in Combustion Systems* (Peters, N. and Rogg B., Ed.), Springer-Verlag, New York, pp. 3-14, 1993.
 - [30]. D'Alessio, A., in *Particulate Carbon: Formation during Combustion* (Siegl, D. C. and Smith, G. W., Ed.), Plenum Press, New York, pp. 207-256, 1981.
 - [31]. Zachariah, M.R., Chin, D., Semerjian, H.G., and Katz, J.L., *Combust. Flame* 78:287 (1989).
 - [32]. Chung, S.L. and Katz, J.L., *Combust. Flame* 61:271 (1985).
 - [33]. Hung, C.H., Miquel, P.F., and Katz, J.L., *J. Mater. Res.* 7:1870 (1992).
 - [34]. Miquel, P.F. and Katz, J.L., *J. Mater. Res.* 9:746 (1994).
 - [35]. Gomez, A. and Rosner, D.E., *Combust. Sci. Technol.* 89:335 (1993).
 - [36]. Waldmann, L. and Schmidt, K. H., in *Aerosol Science* (C.N. Davies, Ed.), Academic Press, New York, pp. 137-162, 1966.
 - [37]. Talbot, L., Cheng, R.K., Schefer, R.W., and Willis, D.R., *J. Fluid Mech.* 101:737 (1980).